


RESEARCH ARTICLE

# Mitigation of flow separation in a highly bent intake duct with active and passive flow control

P. Max<sup>1</sup>, M. Stöbel<sup>1</sup>, D. Kožulović<sup>1</sup> and M. Krummenauer<sup>2</sup>

<sup>1</sup>Department of Aerospace Engineering, Institute of Jet Propulsion, University of the Bundeswehr Munich, Munich, Germany

<sup>2</sup>Bundeswehr Technical Centre for Aircraft and Aeronautical Equipment, Manching, Germany

**Corresponding author:** P. Max; Email: [philipp.max@unibw.de](mailto:philipp.max@unibw.de)

**Received:** 16 November 2023; **Revised:** 23 May 2024; **Accepted:** 27 June 2024

**Keywords:** highly bent engine intakes; active flow control; passive flow control

## Abstract

Typically, the fuselage of a modern military aircraft is designed in such a way that the propulsion system is integrated into it. The main reasons are reduction of installation space and minimisation of radar signature. Those requirements can be achieved by using highly bent engine intakes, which are occluding a direct line of sight to the compressor system. Depending on their design, secondary flows and flow separation can be expected due to the strong curvature of the intake system. In this study, a serpentine intake in front of the Larzac 04 test engine is investigated experimentally and its performance compared with and without flow stabilising measures. In detail, a configuration with vortex generators was compared experimentally with a configuration of active flow control by injected air. In order to analyse and compare the efficiency of both systems, the dimensionless total pressure coefficient, the distortion coefficient (DC60) and detailed surface pressure distributions as well as the aerodynamic interface plane are evaluated. In addition, different throttle lines were recorded for surge line evaluation of the low pressure compressor of the Larzac engine and compared for each flow-stabilising measure investigated. It was found that the application of injecting air showed a larger improvement in surge margin and reduction in distortion coefficients compared to the passive flow control.

## Nomenclature

### Abbreviations

s	– duct	serpentine duct
DC60		distortion coefficient 60°
VG		vortex generator
LPC		low-pressure compressor
HPC		high-pressure compressor
MEIRD		Military Engine Intake Research Duct
DIP		duct inlet plane
DOP		duct outlet plane
AIP		aerodynamic interface plane
CS		cross-section
DOE		design of experiment
ISA		International Standard Atmosphere

### Symbols

$\delta$	boundary layer thickness (m)
$S$	position at the centreline (%)

$x, y, z$	Cartesian coordinates (m)
$L$	length of the MEIRD (m)
$D$	diameter of the duct outlet plane (m)
$c$	vortex generator chord length (m)
$h$	vortex generator height (m)
$p$	pressure (Pa)
$\Pi$	pressure ratio (-)
$n$	spool speed (1/min)
$\dot{m}$	mass flow rate (kg/s)
$SM$	surge margin (-)
$T$	temperature (K)

### **Subscripts**

red	reduced
ref	reference
rel	relative
t	total
AV	average
FAV	face average (total pressure average within the AIP)
amb	ambient
OP	engine operating point

## **1.0 Introduction**

Highly compact diffusers that exhibit high areal diffusion rates and large offsets can improve modern aircraft propulsion systems by enabling lightweight, compact, low-volume intake designs. These engine intakes are typically carried out as so-called serpentine ducts (s-duct). Thereby the severe internal curvature of the s-duct centreline tends to promote cross-flow centrifugal pressure gradients. Such secondary flows create an undesirable non-uniform total pressure distribution and can lead to excessive compressor distortions and engine stall [1, 2]. Flow separation caused by the strong internal contour can also lead to significant engine performance drawbacks. The flow physics concerning distortion in bended ducts and its effects on the compressor performance is similar to those found in ultra-high bypass ratio gas turbine engines equipped with low-speed fans operating under off-design conditions of high incidence or crosswinds [3–5]. However, for a double-bended duct (S-duct) the first bend also develops a pair of counter rotating vortices, which will interact with the ones from the second bend. To minimise the aerodynamic losses occurring in an s-duct, there is still an enormous interest in investigating the effectiveness of various flow stabilising methods and understanding the associated flow phenomena. The flow-stabilising measures are basically classified into velocity profile modifiers, momentum addition to near-wall flow, moving wall configurations and turbulators [6, 7]. Another possible categorisation is into active and passive measures. Thereby, methods are referred as active if they exchange energy with the main flow using an auxiliary device. In contrast, methods that only locally redirect the flow are referred as passive. The advantages of passive methods, especially of vortex generators are their simpler design and easier implementation. Furthermore, they can be subsequently installed in an existing system. The disadvantages are that vortex generators can only be optimised for a specific design point. During other flight phases they are not very efficient and may cause additional parasitic drag. Moreover they pose the risk of foreign object damage (FOD). FOD can both damage the vanes themselves, eliminating their aerodynamic benefit, or cause the vanes to be ingested into the engine. To overcome these shortcomings, there are active control technologies that can be adapted to the individual flight scenario or switched off completely when not needed. However, they require additional energy from the aircraft and are therefore often more complex and expensive than passive measures.

Following Hamstra et al. [8] there are two different concepts for vortex generators. First, a locally limited use of vortex generators at the height of the boundary layer thickness  $\delta$  to control or prevent upcoming flow separation. This approach has been utilised by Tournier et al. [9] and Gissen et al. [10], among others. It offers advantages in experimental investigations, as only spatially limited segments of the intake have to be equipped with vortex generators. The second method is to control the secondary flow [11]. This strategy focuses on influencing the entire inlet flow field by using several rows of (up to 36 [8]) low (20–50% of the boundary layer thickness) vortex generators, also called micro-vanes. Especially for simple, slightly curved intakes with low pressure gradients, micro-vanes turned out to be very effective [11]. In this study, the local approach was chosen because it can be best realised with the existing exchangeable wall elements of the investigated duct. Initial results of the developed vortex generators were discussed in a previous paper [12] and only the best performing configuration is shown here for comparison with the active flow control method.

The active flow-stabilising technologies may be broadly subdivided into suction and injection. While suction pursues the principle of removing low-momentum fluid from the boundary layer, injection should re-energise it. Both measures should enable the boundary layer to withstand higher adverse pressure gradients without separation. Keerthi et al. [13] have investigated suction at various positions in an s-duct and have shown that the lowest distortion parameters are obtained with a suction mass flow rate between 4%–5% of the total inlet mass flow. Furthermore, Keerthi and Kushari [14] compared steady vortex generator jets and suction. They found that the best performance was achieved when both systems were coupled. The improvements were attributed to suction which prevents the flow separation and the vortex generator jets reducing the secondary flow at the same time. Harper et al. [15] used suction, blowing and a combination of both to minimise the flow separation in the intake. The combined effect of blowing and suction is better than either effect considered in isolation. While suction alone and blowing alone showed approximately equivalent effectiveness.

Although many technical papers have been published on active flow stabilising methods implemented in slightly curved s-ducts with circular cross-sections [16, 17] there is still a need to improve the understanding of flow stabilising techniques in more complex shaped intake systems. Literature with active flow control measures investigated in highly contoured double s-bend engine intakes is still very limited. Therefore, in the present paper vortex generators and injection were applied to a double s-duct and the relative improvements in engine performance and flow control effectiveness were evaluated.

## 2.0 Experimental setup

The experiments were performed at the ground-level engine test bed at the Institute of Jet Propulsion, which is capable of testing jet engines with up to 50kN of thrust. This Engine Test Facility (ETF) is a unique test bed in Germany since several engines can be operated for scientific as well as educational purposes [18].

### 2.1 Test vehicle

The Larzac 04 C5 was used as test vehicle (cf. Fig. 1). This engine is the main scientific test engine at this test bed and the Institute of Jet Propulsion has extensive experience with this test vehicle's behaviour under adverse inflow conditions, as well as under compressor stall. And it is equipped with a highly instrumented low-pressure compressor (LPC) and is thus well-suited for investigations of intake-compressor interactions. The most important engine performance data at ISA conditions are listed in Table 1.

### 2.2 Investigated intake and instrumentation

At the Institute of Jet Propulsion, the MEIRD (Military Engine Intake Research Duct) has been designed and manufactured to generate a combined pressure and swirl distortion inside an engine intake and

**Table 1.** Engine performance data at ISA conditions

Parameter	Value
Thrust	13kN
Engine mass flow	27.64kg/s
Spool speed (LPC)	17,500 min <sup>-1</sup>
Spool speed (HPC)	22,561 min <sup>-1</sup>
Pressure ratio (LPC)	2.26
Pressure ratio (HPC)	4.60
Bypass ratio	1.13

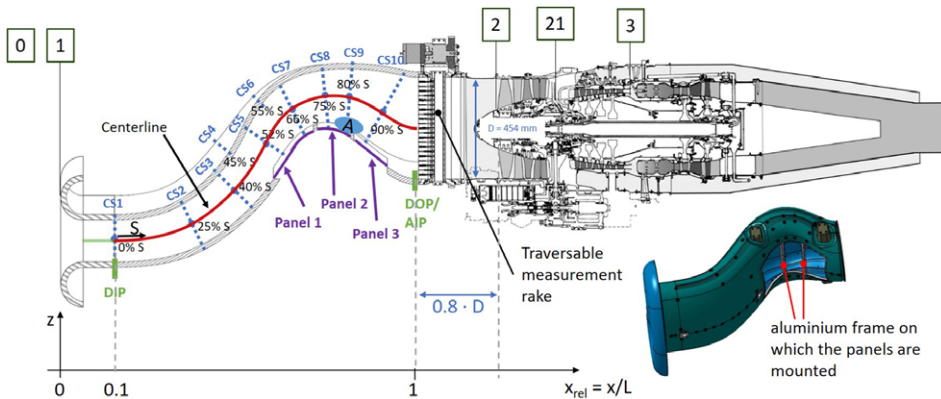


**Figure 1.** Schematic overview of the experimental setup and instrumentation of the MEIRD; 3D-CAD photo of the MEIRD from an angle showing the bottom of the intake; boxes with engine station numbers.

to investigate the flow interaction between duct and compressor both experimentally and numerically [19]. One of the design restrictions was that provoked pressure and swirl distortions at the duct outlet plane (DOP) do not exceed the operating range of the Larzac 04 test vehicle. Figure 1 depicts the entire experimental setup. The traversable measuring rake housing is designed to be as compact as possible such that the DOP and the AIP (aerodynamic interface plane) merge. The axial length of the duct is set to  $3 \cdot D_{DOP}$  (diameter of the duct outlet plane), as this seems to be a reasonable length of a realistic short highly bent intake duct. The fan entry diameter is 454mm ( $D = 454\text{mm}$ ) and the distance between DOP and fan face is  $0.8 \cdot D$ . To achieve the intended strong flow distortion at the AIP the overall inclination of the centreline features a strong curvature. Furthermore, the MEIRD is designed to prevent a direct line of sight on the DOP from the DIP (duct inlet plane), which is an important requirement for low observability military engine systems, in order to reduce the exposure of the highly reflective fan to radar beams. In Fig. 1 information about the basic geometric parameters, as well as the centreline (red) and the positions of the geometry defining cross-sections (CS) are depicted (see also [20]).

The cross-sections are aligned along the centreline (S) in their centres of area. The shape of the cross-sections changes from kidney-shaped ( $S = 0\%$ ) at the DIP to rectangular ( $S = 75\%$ ) to round at the DOP. The different cross-sectional shapes are shown in Fig. 2. In Fig. 2 additionally in CS8 the extent of the blowing slot and the diameter of the DOP is displayed. In the individual cross-sections, as well as in the symmetry plane of the MEIRD, there are static wall pressure probes installed to generate data for flow characterisation, which are analysed in detail in Section 4. Cross-sections four and six are not depicted in Fig. 2, since the static pressure holes are only placed on the upper wall of the duct. Furthermore, a measuring rake was installed at the DOP/AIP, which consists of 10 kiel probes and 11 five-hole pressure

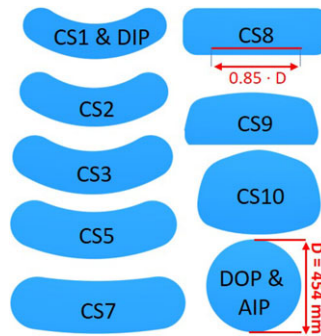


**Figure 2.** Main cross-sections of the MEIRD and sketch of the extend of the blowing slot in CS8.

probes, which are equidistantly distributed along the full span of the rake. Recording the total pressure at the AIP the rake was traversed in either  $6^\circ$  steps or  $60^\circ$  steps in circumferential direction. The measuring rake was only installed during the stationary operation of the engine, but not during the recording of the intake-compressor map. This was mainly due to prevention of damage to the traversing system by compressor surge events.

The CFD investigations by Haug et al. [20] did already show that the MEIRD features a separation area located at its second bend (cf. Fig. 1 area ‘A’). To investigate this area of flow separation in special detail and to provide the ability to influence it with both active and passive measures, the MEIRD has three exchangeable panels in this region. While panel 1 is placed upstream of the detachment bubble, panel 2 is positioned exactly on it and panel 3 is partly still located at the detachment area and partly downstream of the flow detachment. With the aim of suppressing the separation area and improving the overall performance of the system three different configurations were investigated and compared in this study:

- *Baseline*: MEIRD without flow stabilising measures (Reference case).
- *VG*: Only panel 1 is replaced by a panel with vortex generators (cf. Fig. 3).
- *Blo*: Panel 1 and 3 as in the Baseline case. Only panel 2 is replaced by a panel with an integrated Coanda nozzle for active flow stabilisation by injection (cf. Fig. 3).

Both the VG configuration and the Blo configuration have been extensively investigated specifically for the MEIRD in preliminary tests either numerically in a DOE (design of experiment) study [12] or experimentally in a scaled setup [21]. This means that they are technically well-developed variants that have already achieved promising results in previous testing and are not first-time developments.

The vortex generator panel with the most relevant geometric parameters, as well as a cutaway view of the blowing configuration panel, is shown in Fig. 3.

The vortex generator height ( $h_{VG}$ ) in relation to the reference boundary layer thickness  $\delta_{ref}^1$  is 1.3. The VG chord length ( $c$ ) referred to reference boundary layer thickness is 9.3. And the y-distance over the reference boundary layer thickness is 2.8. When the blowing configuration was applied to the MEIRD, the blowing mass flow rate has been increased from 1% in 0.5% steps to 2%. The injection mass flow rate was always related to the respective intake inlet mass flow rate. During the blowing experiments the injection mass flow was provided by an external compressor. The extent of the blowing slot in y-direction was kept constant at  $0.85 \cdot D$  (cf. Fig. 2 CS8).

<sup>1</sup>The boundary layer thickness on the bottom of the MEIRD within CS3 at  $n_{red,rel} = 90\%$  is used as reference value  $\delta_{ref}$ .

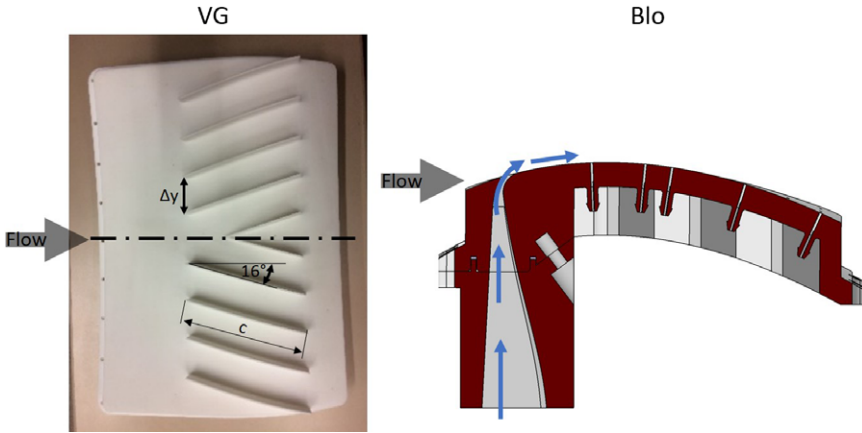


**Figure 3.** Vortex generator configuration (top view) with geometry parameters; blowing configuration (cutaway view) with Coanda nozzle.

**3.0 Definitions**

All pressure data used for flow characterisation and evaluation of the effects of the different flow control configurations are presented as relative values. Both the static wall pressure

$$p_{rel} = \frac{P_{static,wall}}{P_{amb}} \tag{1}$$

measured along the duct surface as well as the total pressure

$$P_{t,rel} = \frac{P_{total}}{P_{amb}} \tag{2}$$

are evaluated in relation to the ambient pressure  $p_{amb}$  at the engine test cell.

To compare the performance of the individual configurations, both the distortion parameters defined in SAE standard 1420 [22] and certain engine parameters were used. Their definitions are given in the following sections.

**3.1 Distortion descriptors**

The first parameter described is the pressure recovery which gives an overall impression on the performance of an intake system.

$$PR = \left(1 - \frac{P_{t,AV-DOP}}{P_{t,amb}}\right) \cdot 100\% = \left(1 - \frac{P_{t,FAV}}{P_{t,amb}}\right) \cdot 100\% \tag{3}$$

A further well-known distortion coefficient is the DC60 parameter:

$$DC60 = \max_{60^\circ} \left( \frac{P_{t,FAV} - P_{t,Worst-60^\circ}}{P_{t,FAV} - p_{AV}} \right), \tag{4}$$

where  $P_{t,FAV}$  is the face average total pressure of the AIP.  $P_{t,Worst-60^\circ}$  is the mean of the measurement points in a sector of 60° with the lowest total pressure values. And  $p_{AV}$  is the average static pressure in the AIP. The DC60 distortion coefficient was first defined by Reid [23].

The circumferential distortion intensity (CDI) at the  $k^{th}$  radial location (“ring”) is defined as [22]

$$CDI_k = \max_k \left( \frac{P_{t,AV} - P_{t,AV-LOW}}{P_{t,AV}} \right), \tag{5}$$

where  $P_{t,AV}$  is the ring averaged total pressure and  $P_{t,AV-LOW}$  is the subset of only those values that are lower than  $P_{t,AV}$  ( $P_{t,AV-LOW} < P_{t,AV}$ ). The maximum of  $k$  rings indicates the highest circumferential distortion intensity.

### 3.2 Engine parameters

Several parameters are introduced to evaluate the performance and behaviour under distorted inflow of the test vehicle. The reduced engine mass flow is given as [24]:

$$\dot{m}_{red} = \dot{m} \cdot \frac{P_{ISA}}{p_{t1}} \cdot \sqrt{\frac{T_{t1}}{T_{ISA}}} \quad (6)$$

The reduced spool speed of the low-pressure compressor [24]:

$$n_{red} = n \cdot \sqrt{\frac{T_{ISA}}{T_{t1}}} \quad (7)$$

The intake-compressor pressure ratio

$$\Delta p_{t(1,21)} = \frac{p_{t,21}}{p_{t1}} \quad (8)$$

The intake-compressor pressure ratio  $\Delta p_{t(1,21)}$  is defined as the ratio between the LPC core outlet pressure  $p_{t,21}$  and the intake inlet total pressure  $p_{t1}$ . This means that the intake-compressor system is considered as one single unit.

The definition of the surge margin is [25]:

$$SM = \frac{\Pi_{t,SM} \cdot \dot{m}_{OP}}{\Pi_{t,OP} \cdot \dot{m}_{SM}} - 1 \quad (9)$$

Where  $\dot{m}_{OP}$  and  $\dot{m}_{SM}$  are reduced mass flow rates. The surge margin definition is used for constant reduced spool speed.

### 3.3 Swirl angles

According to the SAE Standard 5686 [26] swirl can be grouped into four categories: (1) bulk swirl, (2) tightly wound vortices, (3) paired swirl and (4) cross-flow swirl. Examples on the generation of each type of swirl and how the swirl is formed is also given in the SAE standard. The characteristics of each type of swirl will be illustrated in terms of the swirl angle (cf. Fig. 4). The swirl angle  $\alpha$  is defined at a point as the circumferential angle of flow from the axial direction as calculated in Equation (10) and shown in Fig. 4.

$$\alpha = \tan^{-1} (v_\alpha / v_x) \quad (10)$$

## 4.0 Results

In the following, the results from the static wall pressure boreholes (centreline, panels and cross-sections) are described and analysed. Furthermore, the measuring rake (five-hole pressure probes and kiel probes) results are presented. The intake-compressor map is also discussed. All results refer to the 76% speed line. The presentation of the results at this speed line was chosen because in the range between 60%–86% a larger surge margin is particularly important when accelerating the engine. Therefore, it is a major ambition to achieve a higher surge margin, especially in this range. The 76% speed line is used as a point of reference for this purpose.

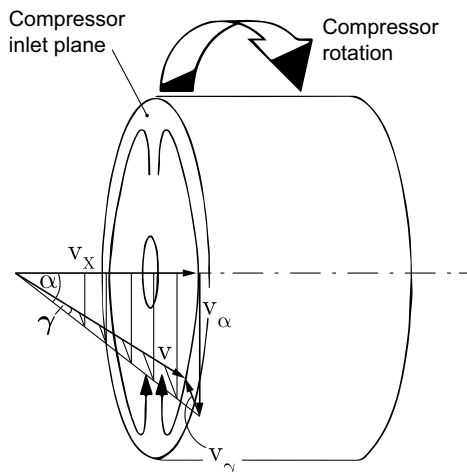


**Figure 4.** Definition of swirl angles.

#### 4.1 Static pressure measurements along intake centreline ( $x$ - $z$ plane)

First, the intake without flow stabilising measures was investigated. This baseline case serves on the one hand for the flow characterisation of the intake and on the other hand as a reference to evaluate and assess the efficiency of the active and passive flow control measures. For this reason, the static wall pressures at the upper wall centreline (top, continuous lines) and lower wall centreline (bot, dashed lines) in the symmetry plane (grey, MEIRD contour) of the intake were recorded (cf. Fig. 5). The graphs shown in Fig. 5 were evaluated at a constant engine speed of  $n_{red,rel} = 76\%$ . Furthermore, the injection mass flow rate for the Blo configuration was set to 1.5%. This turns out to be the optimal injection mass flow rate from a performance point of view, as will be explained in more detail later in Section 4.4. The results and conclusions given at  $n_{red,rel} = 76\%$  can generally be applied to the speed range between  $n_{red,rel} = 54\%$  and  $n_{red,rel} = 86\%$ . Figure 5 further shows the relative  $x$ -position of the detachment bubble (A), as well as the  $x_{rel}$  position of the individual panels. The relative  $x$ -axis is referred to the total length  $L$  of the intake (cf. Fig. 1). Additionally, the position of the injection (red arrow) is depicted.

The static pressure curves at the upper wall of the MEIRD are largely identical. In the area between  $x_{rel} = 0.1$  and  $x_{rel} = 0.7$ , the static wall pressure of the VG configuration is lower than that of the Baseline and Blo configurations. At  $x_{rel} = 0.95$ , thus in the region of the DOP, the Blo configuration possesses the highest static pressure, followed by the VG configuration. The Blo and the VG configuration achieve higher static pressure levels at the DOP than at the DIP. While the static pressure of the baseline configuration is lower at the DOP than at the DIP.

The lower wall static pressure curves show up almost identical pressure values between  $x_{rel} = 0.1$  and  $x_{rel} = 0.68$ . Between  $x_{rel} = 0.76$  and  $x_{rel} = 0.86$ , the baseline configuration shows an apparent pressure plateau on the lower wall, which can be attributed to the separation area (A) [20]. At the VG configuration as well as for the Blo configuration, a pressure plateau is no longer present. Looking at the Blo and VG configuration the static wall pressure increases continuously from  $x_{rel} = 0.73$  up to the DOP. The baseline inlet separates, whilst the VG and Blo configuration still maintain diffusion to the DOP.

The VG and the Blo configuration reach a higher static pressure at the DOP than at the DIP. Based on the analysis of the static wall pressure characteristics, it is evident that both flow-stabilising measures effectively suppress the separation bubble. According to the static pressures at the AIP the Blo configuration features a higher static pressure level than the VG-configuration and therefore the LPC is exposed to a higher static pressure level and its performance is better (cf. Fig. 12). This is due to the higher and



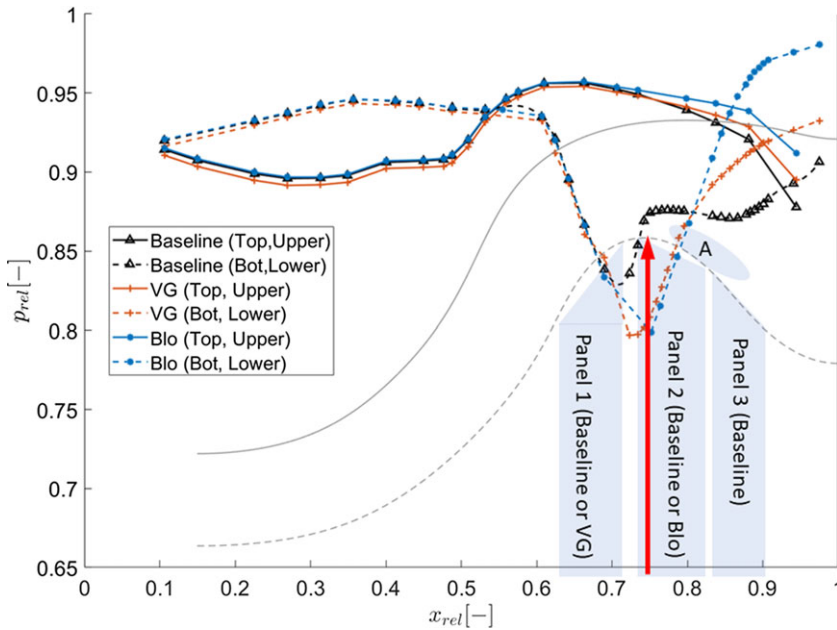


**Figure 5.** Static wall pressure at the  $zx$ -symmetry plane at  $n_{red,rel} = 76\%$ ,  $\dot{m}_{Blo} = 1.5\%$ .

more uniform static and total pressure distribution in front of the LPC. The pressure loss through the intake is consequently lowest using the Blo configuration (compare total pressure in the AIP at Fig. 9(c) and (a)).

#### 4.2 Static pressure variation along $x$ - $y$ plane

The wall pressure data along the centreline ( $y_{rel} = 0$ ) provide initial knowledge that the flow stabilisation measures are effectively suppressing the detachment bubble. However, the data refer exclusively to the  $z$ - $x$  plane and do not provide any information about the  $x$ - $y$  plane. Therefore additional static pressure holes were positioned along the  $x$ - $y$  plane of Panel 2 and 3 to investigate the 3D effects of the VG and Blo configuration, shown in Fig. 6. The panels are attached to the aluminium frame integrated into the MEIRD (cf. Fig. 1). The transition between the panels and the MEIRD is aerodynamically smooth. However, due to the aluminium frame, measuring points in the junction between the individual panels are missing, which leads to a static pressure step in the wall pressure distribution displayed in Fig. 6.

Figure 6 shows the results of the individual configurations.  $Y_{rel}$  is related to the intake outlet diameter and the engine speed was kept constant at  $n_{red,rel} = 76\%$ . The blowing mass flow rate was  $1.5\%$ . Looking at the baseline configuration, the detachment line is clearly visible on panel 2 in a ‘C’ shape. Between  $x_{rel} = 0.76$  and  $x_{rel} = 0.78$  the flow detaches. The complete panel 3 is detached ( $p_{rel} = 0.82$  cf. Fig. 5 pressure plateau (A)).

The VG configuration shows its impact especially on P2 in the way of a static pressure drop which accelerates the flow. However, the flow is accelerated much stronger at  $y_{rel} = 0$  than in the outer regions at  $y_{rel} = \pm 0.35$ . On P3, the static wall pressure continues to increase continuously and homogeneously.

The Blo configuration depicts a strong acceleration on P2 which is clearly visible in the static pressure drop. At  $y_{rel} = \pm 0.37$  an area with higher static pressure can be observed. In these two areas, the Coanda nozzle was fixed by two struts to prevent the injection slot from widening during the tests. Due to these struts, no injection was possible in this area. P3 shows a massive continuous pressure increase for the injection configuration.

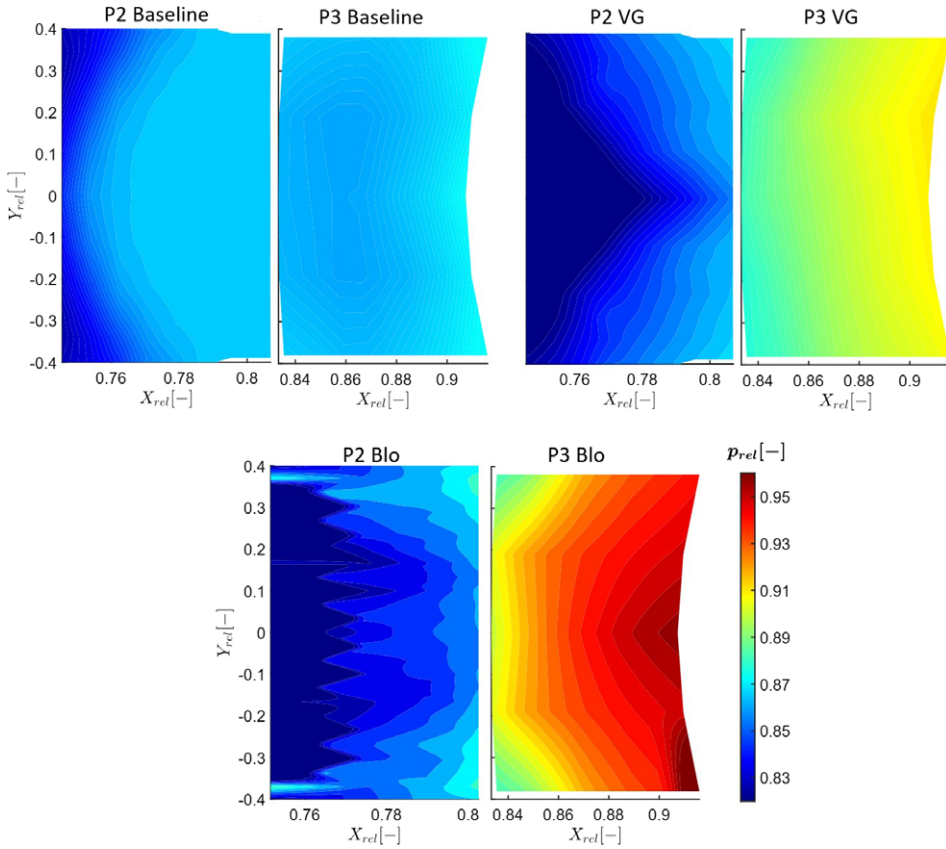


**Figure 6.** Static wall pressure on panel 2 and 3 for the different investigated configurations at  $n_{red,rel} = 76\%$ ,  $\dot{m}_{Blo} = 1.5\%$ .

The analysis of the surface plots confirms the statements already made regarding the wall pressure curves in the symmetry plane. The further pressure increase on P3 is more pronounced in the Blo configuration than in the VG configuration ( $p_{rel,p3,max,Blo} = 0.97$ ;  $p_{rel,p3,max,VG} = 0.92$ ).

### 4.3 Static pressure variation around wall

To further understand the static pressure rises and drops within the MEIRD, the static wall pressure curves in the individual cross-sections were evaluated. From cross-section 1 to 7, the baseline configuration and the Blo configuration are almost identical. At CS5, at  $y/d = 0.8$  the blowing configuration shows a slightly higher static pressure than the baseline configuration does.

It is to note, that the VG configuration in cross sections 1-6 has an overall lower static pressure level than the other two configurations. This effect was already observed in Fig. 5 when analysing the centreline pressure curves. The vortex generators provide a slight acceleration of the flow in CS 1-6. In CS7 just before the detachment bubble, all three configurations are almost identical. In CS8, the baseline configuration shows the familiar pressure plateau of the detachment bubble. The pressure curve of the blowing configuration could not be recorded completely due to the Coanda nozzle slot placed in this area. In CS9, the Blo configuration shows a significant acceleration on the lower wall area, while reaching already a higher static pressure level than the other two configurations at the upper wall of the MEIRD. The VG configuration shows an asymmetry at the bottom in CS9, which can also be observed in the

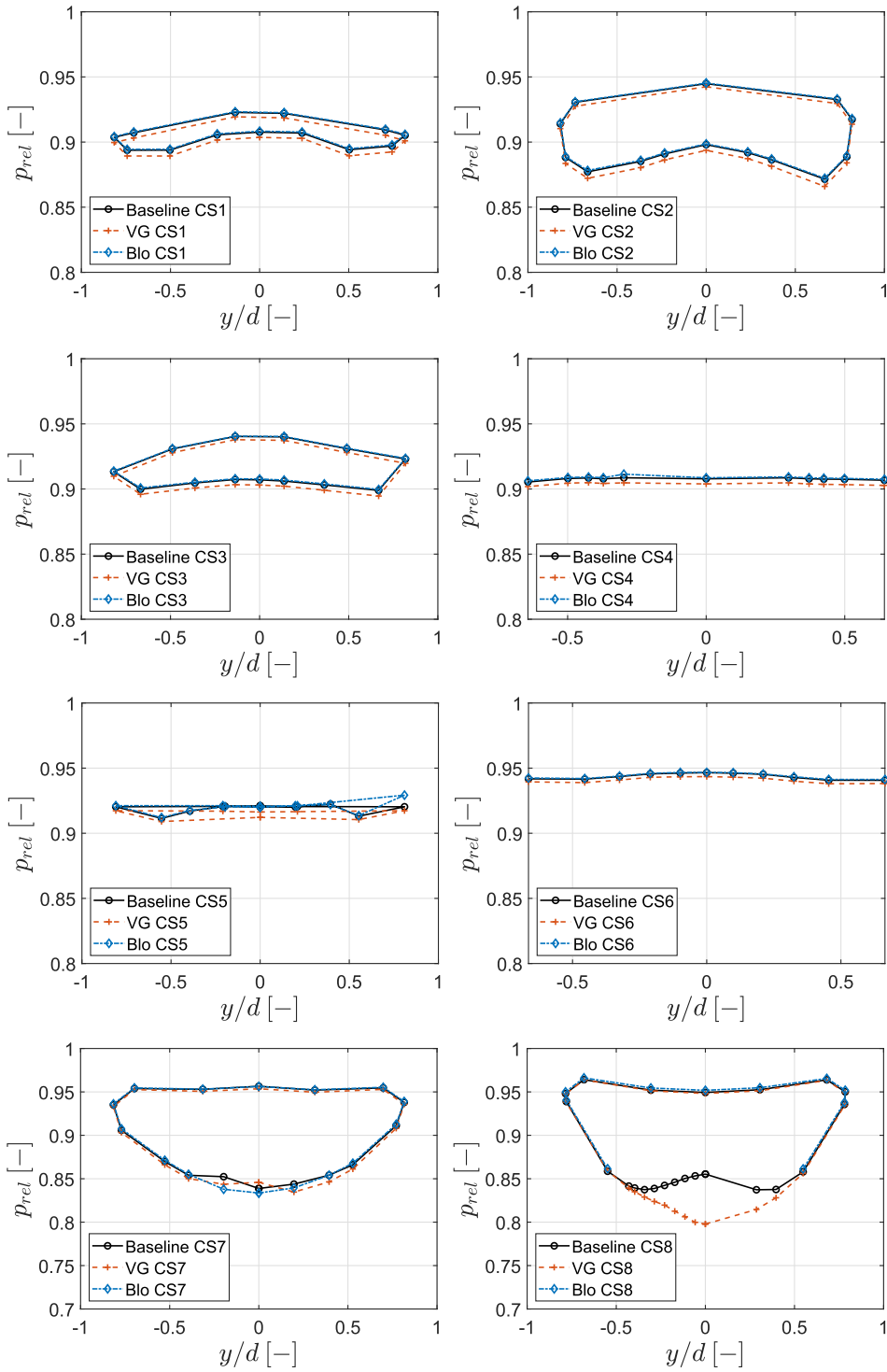
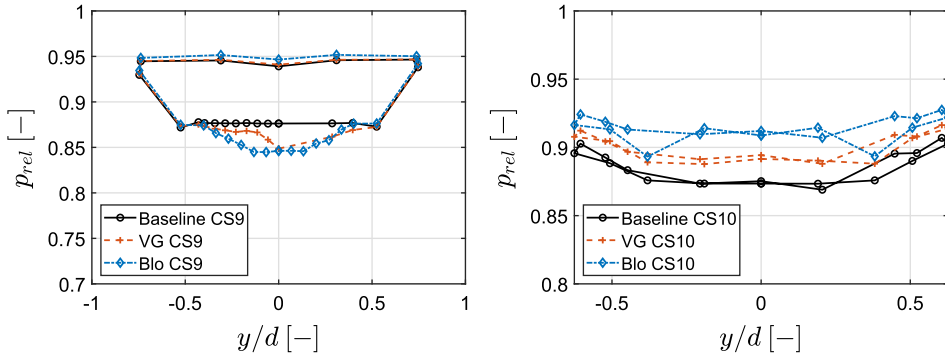


Figure 7. Static wall pressure on the different cross-sections at  $n_{red,rel} = 76\%$ ,  $\dot{m}_{Blo} = 1.5\%$ .



**Figure 8.** Static wall pressure on the different cross-sections at  $n_{red,rel} = 76\%$ ,  $\dot{m}_{Blo} = 1.5\%$ .

analyses of the AIP plots. As expected, the Blo configuration shows the highest static pressure recovery in CS10.

#### 4.4 LPC inlet flow field

The results of the total pressure measured with the Kiel probes of the measuring rake are displayed in Fig. 9. Thereby, an immense total pressure distortion at the  $180^\circ$  position occurs in the baseline configuration (Fig. 9(a)). This total pressure distortion is caused by the detachment bubble. Furthermore, two total pressure disturbances are slightly visible at the  $60^\circ$  and  $300^\circ$  positions. These disturbances are caused by the vortex system which arises in the first bend of the MEIRD [20]. The distortion parameters for the baseline configuration and the other configurations are listed in Table 2. At an engine speed of  $n_{red,rel} = 76\%$ , the DC60 parameter of the baseline configuration is 0.9, which is too high for most engine manufacturers. An injection mass flow rate of 1%, reduces the extent of the total pressure disturbance (cf. Fig. 9(b)). However, the dominant core of the distortion at  $180^\circ$  is still present. Nevertheless, the DC60 is reduced to 0.3. As only the lower wall of the MEIRD is equipped with flow stabilising measures the pair of vortices at  $60^\circ$  and  $300^\circ$  are prominent in all configurations. With an injection mass flow of 1.5%, the total pressure disturbance at  $180^\circ$  is completely suppressed (Fig. 9(c)). A further increase of the mass flow to 2% causes no improvement (Fig. 9(d)). In contrast, at 2% injection mass flow,  $p_{t,rel}$  is above one at the  $180^\circ$  position, which again can be considered as a distortion onto the compressor system. Due to the limited time at which the injection mass flow of the external compressor is available, the blowing AIP plots are very coarsely resolved. The buffered injection air from the external compressor is not sufficient to finely traverse the measuring rake including sufficient measuring time. Therefore, the corresponding distortion parameters are also shown in brackets in Table 2. Nevertheless, a qualitative statement can be made. The total pressure plot of the VG configuration is shown in Fig. 9(e)). The total pressure disturbance at  $180^\circ$  is weakened and stretched in width. However, the total pressure disturbance is best suppressed in the injection configuration with 1.5% blowing mass flow.

In addition to the Kiel probes, the five-hole pressure probes in the measuring rake have also been evaluated [27]. The results in circumferential direction ( $\alpha$ -angle) are shown in Fig. 10.

A positive  $\alpha$ -angle indicates a counterclockwise flow and vice versa. Figure 10(a) depicts the  $\alpha$ -angle in the baseline case. The two opposite flow directions in the right and left halves of the AIP are evident. The maximum flow angles reach  $\pm 30^\circ$ . At the  $180^\circ$  position the two vortices meet. At  $200^\circ$  and respectively at  $175^\circ$  two additional pairs of vortices running in opposite directions occur. The flow stabilising measures in the MEIRD reduce the flow angles (cf. Fig. 10(b), (c)). In the case of the VG configuration the maximal flow angles are reduced to  $\pm 15^\circ$  (Fig. 10(c)). During injection, the flow angles are further reduced and the circumferential swirl in the AIP decreases (Fig. 10(b)).

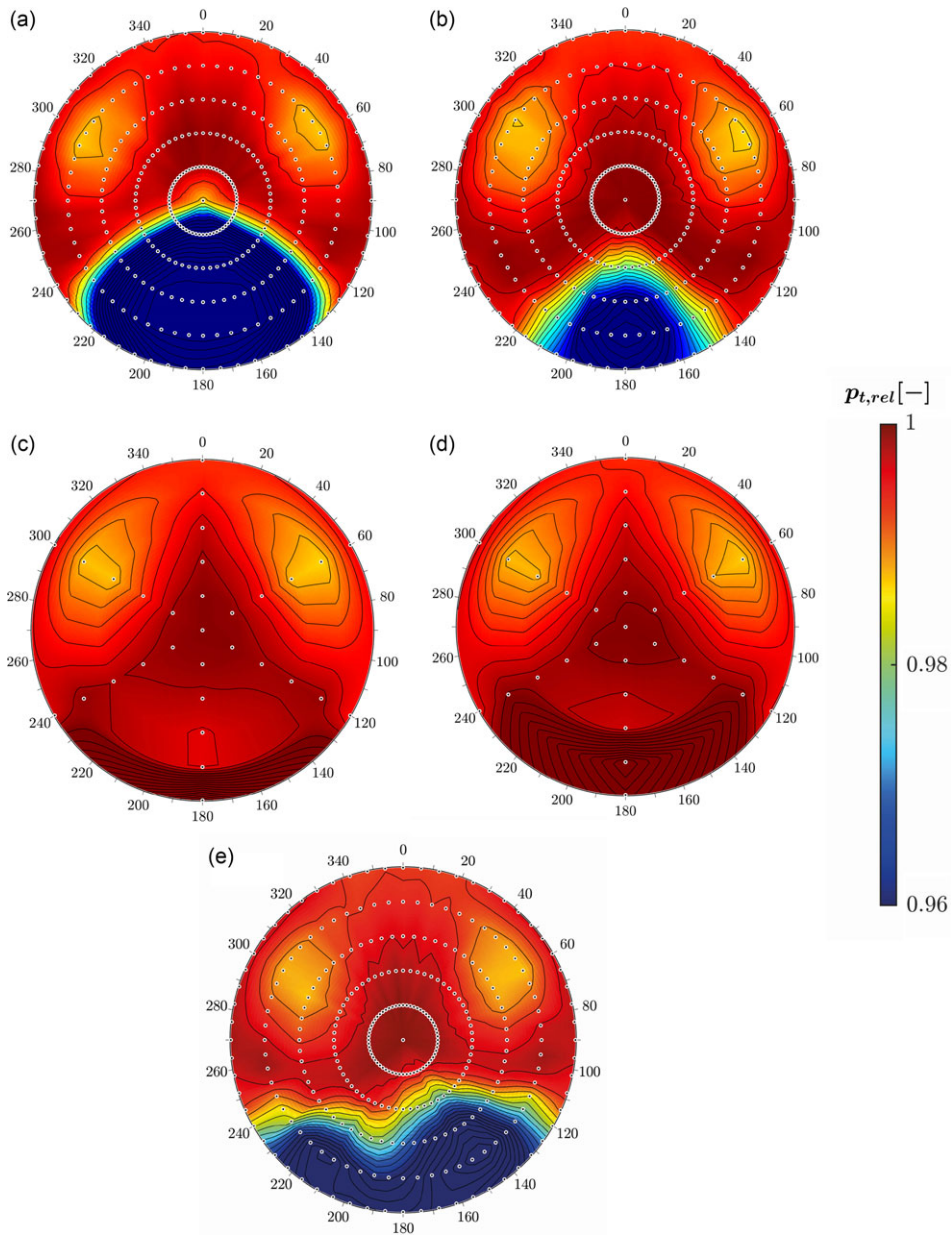


**Figure 9.** Total pressure within the AIP at  $n_{red,rel} = 76\%$ , (a) baseline configuration, (b) Blo configuration with  $\dot{m}_{Blo} = 1\%$ , (c) Blo configuration with  $\dot{m}_{Blo} = 1.5\%$ , (d) Blo configuration with  $\dot{m}_{Blo} = 2\%$ , (e) vortex generator (VG) configuration.

Considering the radial flow direction ( $\gamma$ -angle cf. Fig. 11), a positive  $\gamma$ -angle means a flow towards the centre of the AIP.

In all investigated configurations, it can be seen that the flow in the upper half of the AIP moves outwards and in the lower half towards the centre. With installed flow-stabilising measures, the maximal flow angles in the radial direction are reduced. To sum up, it might be possible to derive the flow direction within the AIP from the Kiel total pressure measurements data. The fluid moves in the circumferential

**Table 2.** Distortion coefficients and surge margin

		$n_{red,rel} = 54\%$	$n_{red,rel} = 76\%$	$n_{red,rel} = 86\%$
Baseline	PR (%)	1.18	2.66	3.60
	CDI (-)	0.027	0.067	0.088
	DC60 (-)	0.45	0.46	0.45
	SM (-)	15.74	12.50	10.21
VG	PR (%)	0.46	1.07	1.63
	CDI (-)	0.012	0.029	0.044
	DC60 (-)	0.28	0.3	0.29
	SM (-)	14.78	13.76	11.26
Blo ( $\dot{m}_{Blo} = 1.5\%$ )	PR (%)	0.15	(0.32)	(0.50)
	CDI (-)	0.002	(0.005)	(0.006)
	DC60 (-)	0.05	(0.05)	(0.05)
	SM (-)	18.13	18.49	18.60

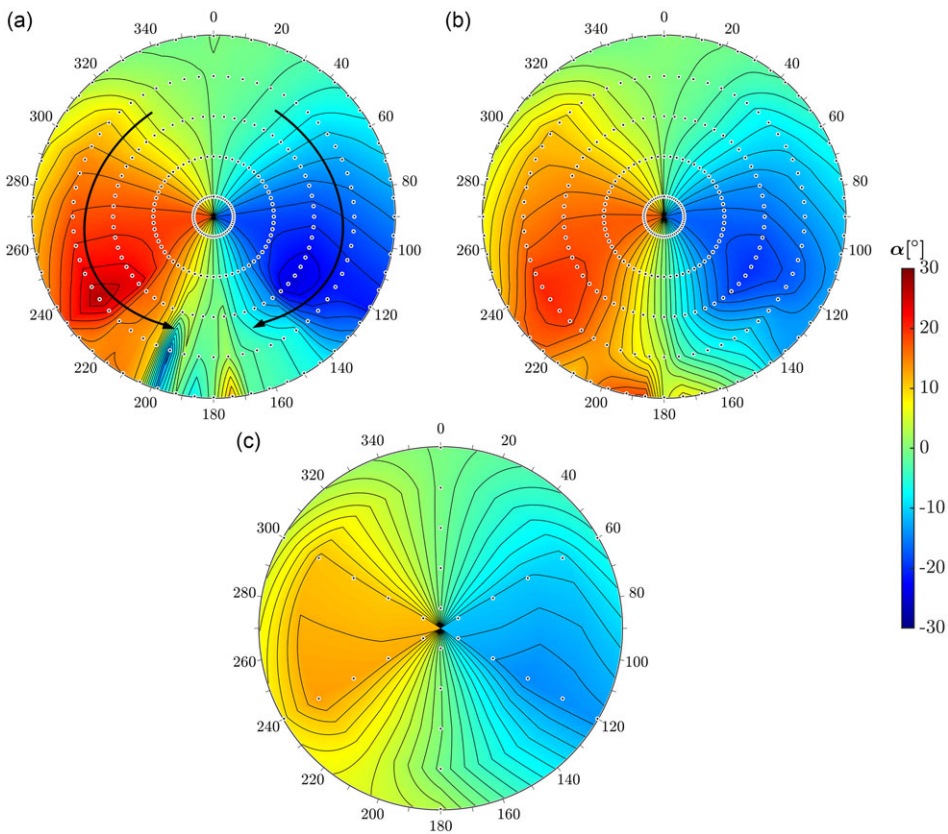


**Figure 10.** Swirl in circumferential direction in the AIP at  $n_{red,rel} = 76\%$ ; (a) baseline configuration, (b) VG configuration, (c) Blo configuration with  $\dot{m}_{Blo} = 1.5\%$  (positive rotation: counterclockwise direction).

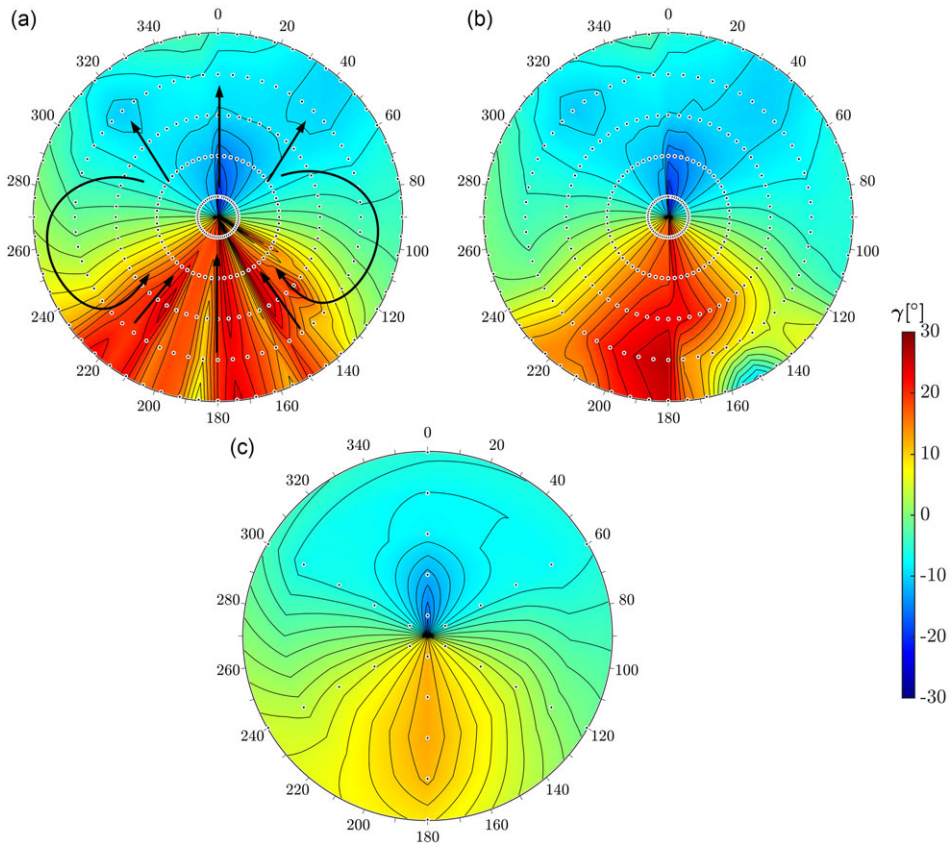


**Figure 11.** Swirl in radial direction in the AIP at  $n_{red,rel} = 76\%$ ; (a) baseline configuration, (b) VG configuration, (c) Blo configuration with  $m_{Blo} = 1.5\%$  (positive: to the centre point).

direction from the higher pressure level to the lower pressure level. This physical aspect is confirmed by the results of the five-hole pressure probes. The effects of the duct onto the fan and the mitigation of the flow separation due to the investigated measures can be summarised in the following steps:

1. When coupled to the baseline inlet, the fan ingests low total pressure at  $180^\circ$ .
2. Fan responds by reducing inlet static pressure at  $180^\circ$  (Fig. 5 at  $x/L = 1.0$ ).
3. Static pressure gradients drive flow from upper to lower half of intake.
4. Flow migration generates swirl and radial flow distortion (Figs 10(a) and 11(a)).
5. Vortex generator and injector methods reduce total pressure distortion, which in turn weakens the fan response and top-to-bottom static pressure gradients [4, 5].
6. This reduces inlet swirl and radial flow distortion entering the fan.
7. Fan performance rises.

#### 4.5 Intake-compressor map

To assess the effects of the intake disturbances on the compressor system, the intake-low-pressure compressor map has been recorded (Fig. 12). From a reduced relative speed of 54% up to the maximum

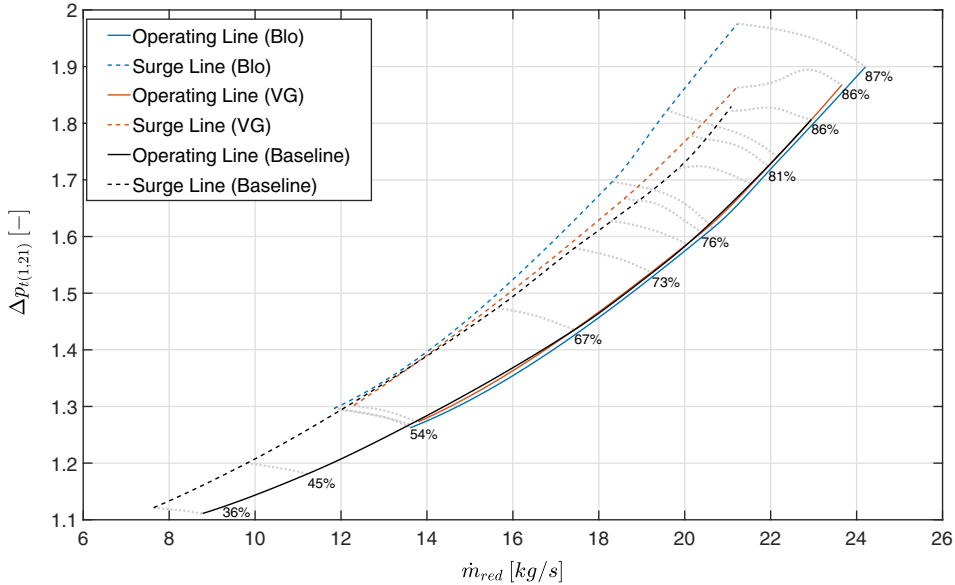


**Figure 12.** Intake-compressor map for the different investigated configurations ( $\dot{m}_{Blo} = 1.5\%$ ).

speed of around 86%, the flow-stabilising measures expand the map and increase the safe operating range compared to the baseline case. This increases the surge margin as listed in Table 2. Thereby, the injection configuration features the largest surge margin from a reduced relative speed of 62% up to the maximal measured spool speed (cf. Fig. 12). Table 2 demonstrates that a reduction of the distortion parameters increases the surge margin. With a DC60 value of 0.05, the Blo configuration exhibits a surge margin of 18.49 at  $n_{red,rel} = 76\%$ . Corresponding to an increase of 48% in the surge margin compared to the baseline configuration. For the same operating point, the VG configuration improves the surge margin by 10% compared to the baseline configuration. Both flow stabilisation measures, reduce the PR and the CDI parameters significantly. Whereby the Blo configuration achieves even lower distortion parameter values compared to the VG configuration. For instance, the DC60 parameter at  $n_{red,rel} = 76\%$  is reduced from 0.9 at the baseline configuration to 0.35 with the VG configuration to 0.05 using the Blo configuration.

## 5.0 Conclusions and outlook

Vortex generators and active injection to suppress flow separation were successfully implemented and measured on a highly contoured engine intake as well as in terms of efficiency compared to each other. The results show that both the vortex generators and the injection reduce the distortion parameters in the aerodynamic interface plane and expand the safe operating range of the intake-low-pressure compressor map. Further the active injection is predominant over the vortex generators in all aspects. Thereby, an injection mass flow rate of 1.5% in relation to the intake inlet mass flow is sufficient to reduce the distortion parameters and to increase the intake-compressor performance. A further increase of the blowing mass flow rate does not lead to a further reduction of the distortion parameters. The investigated vortex generator configuration was optimised prior in a design of experiment study and featured a vortex generator height of 1.3 related to the boundary layer thickness. The results demonstrate that for a reduced relative engine speed of 76%, the vortex generators reduce the DC60 disturbance parameter by 61% and the injection configuration with a mass flow rate of 1.5% reduces the DC60 value by 94% compared to no flow stabilising measure applied. Reducing the DC60 parameter simultaneously increases the surge



margin. In relation to the baseline configuration, using the vortex generators increases the surge margin by 10.1% and by 48% with the blowing configuration installed. The homogenisation of the compressor inflow significantly increases the surge margin and thus the performance of the intake-compressor system. Furthermore, the results show that by suppressing the separation bubble in the intake, the secondary flow effects become more prominent.

The demonstrated results indicate the potential of implementing active flow-stabilising measures in a highly contoured engine intakes. In s-shaped intakes, the naturally occurring static wall pressure difference can often be utilised for the recirculation of air within the intake to support active flow stabilising measures and to reduce their amount of required energy. Managing this naturally occurring pressure difference for active flow stabilisation can further reduce the energy demand of the active measures and further increase the overall system performance.

**Acknowledgements.** The authors gratefully acknowledge the financial support of the Bundeswehr Technical Centre for Aircraft and Aeronautical Equipment which funded this research project on investigations of serpentine engine intakes.

## References

- [1] Guo, R.W. and Seddon, J. The swirl in an s-duct of typical air intake proportions, *Aeronaut. Q.*, 1983, **340**, (2), pp 99–129.
- [2] Tindell, R.H. Highly compact inlet diffuser technology. *Journal of Propulsion and Power*, 1988, **40**, (6), pp 557–563.
- [3] Vadlamani, N.R., Cao, T., Watson, R. and Tucker, P.G. Toward future installations: mutual interactions of short intakes with modern high bypass fans, *J. Turbomach.*, 2019, **141**, (8), p 081013.
- [4] Wakelam, C.T., Hynes, T.P., Hodson, H.P., Evans, S.W. and Chanez, P. Separation control for aero engine intakes, part 2: high-speed investigations, *J. Propul. Power*, 2012, **280**, (4), pp 766–772.
- [5] Carnevale, M., Wang, F., Green, J.S. and Di Mare, L. Lip stall suppression in powered intakes, *J. Propul. Power*, 2016, **320**, (1), pp 161–170.
- [6] Gad-el Hak, M. and Bushnell, D.M. Separation control, 1991.
- [7] Gad-el Hak, M. Modern developments in flow control, *Appl. Mech. Rev.*, 1996, **490**, (7), pp 365–379. ISSN 0003-6900. doi: [10.1115/1.3101931](https://doi.org/10.1115/1.3101931)
- [8] Hamstra, J., Miller, D., Truax, P., Anderson, B. and Wendt, B. Active inlet flow control technology demonstration, *Aeronaut. J.*, 2000 doi: [10.1017/S0001924000091971](https://doi.org/10.1017/S0001924000091971)
- [9] Tournier, S., Paduano, J. and Pagan, D. Flow control in a transonic inlet, 36th AIAA Fluid Dynamics Conference and Exhibit, 2006, p 3883.
- [10] Gissen, A.N., Vukasinovic, B., McMillan, M.L. and Glezer, A. Distortion management in a boundary layer ingestion inlet diffuser using hybrid flow control, *J. Propul. Power*, 2014, **300**, (3), pp 834–844.
- [11] Anderson, B.H. and Gibb, J. Study on vortex generator flow control for the management of inlet distortion, *J. Propul. Power*, 1993, **90**, (3), pp 422–430.
- [12] Kächele, T., Rademakers, R., Stöbel, M. and Niehuis, R. Cfd based optimization of vortex generator flow control in a highly bent intake geometry using design of experiments, 2018 AIAA Aerospace Sciences Meeting. doi: [10.2514/6.2018-0407](https://doi.org/10.2514/6.2018-0407)
- [13] Keerthi, M.C., Kushari, A. and Somasundaram, V. Experimental study of suction flow control effectiveness in a serpentine intake, *J. Fluids Eng.*, 2017, **1390**, (10). ISSN 0098-2202. doi: [10.1115/1.4036827](https://doi.org/10.1115/1.4036827)
- [14] Keerthi, M.C. and Kushari, A. Effectiveness of vortex generator jets and wall suction on separated flows in serpentine-duct diffuser, *Aerospace Sci. Technol.*, 2014, **34**, pp 12–19. ISSN 12709638. doi: [10.1016/j.ast.2014.01.013](https://doi.org/10.1016/j.ast.2014.01.013)
- [15] Harper, D., Leitch, T., Ng, W., Guillot, S. and Burdisso, R. Boundary layer control and wall-pressure fluctuations in a serpentine inlet, 36th AIAA/ASME/SAE/ASEE Joint Propulsion Conference and Exhibit, 2000, p 3597.
- [16] Wellborn, S.R., Reichert, B.A. and Okiishi, T.H. Study of the compressible flow in a diffusing s-duct, *J. Propul. Power*, 1994, **100**, (5), pp 668–675.
- [17] Wellborn, S.R., Reichert, B.A. and Okiishi, T.H. An experimental investigation of the flow in a diffusing s-duct, 28th Joint Propulsion Conference and Exhibit, 1992, p 3622.
- [18] Bindl, S., Muth, B. and Niehuis, R. Experimental investigations on macro-aerodynamics within a jet engine ground test facility, 45th AIAA/ASME/SAE/ASEE Joint Propulsion Conference & Exhibit, Reston, Virginia, 08022009. American Institute of Aeronautics and Astronautics. ISBN 978-1-60086-972-3. doi: [10.2514/6.2009-4828](https://doi.org/10.2514/6.2009-4828)
- [19] Rademakers, R.P.M., Haug, J.P., Niehuis, R. and Stöbel, M. Design and development of a military engine inlet research duct, 2016 30th Congress of the International Council of the Aeronautical Sciences. Deajeon, Korea.
- [20] Haug, J.P., Rademakers, R.P.M., Stöbel, M. and Niehuis, R. Numerical flow field analysis in a highly bent intake duct, Volume 2B: Turbomachinery. American Society of Mechanical Engineers, 2018. ISBN 978-0-7918-5100-5. doi: [10.1115/GT2018-76633](https://doi.org/10.1115/GT2018-76633)
- [21] Max, P., Stöbel, M., Krummenauer, M. and Reinhard, N. Effectiveness of active flow control techniques in an advanced s-shaped engine intake, GPPS 2021. doi: [10.33737/gpps21-tc-102](https://doi.org/10.33737/gpps21-tc-102)
- [22] S-16 Turbine Engine Inlet Flow Distortion Committee. Gas turbine engine inlet flow distortion guidelines, a.

- [23] Reid, C. (Ed) The response of axial flow compressors to intake flow distortion, ASME 1969 Gas Turbine Conference and Products Show of Turbo Expo: Power for Land, Sea, and Air, 1969. doi: [10.1115/69-GT-29](https://doi.org/10.1115/69-GT-29)
- [24] Luftfahrttechnisches handbuch (lth). Ottobrunn: LTH - Koordinierungsstelle, 2014.
- [25] Dudgeon, E. Guide to the measurement of the transient performance of aircraft turbine engines and components: Agard-ar-320, 1994.
- [26] S-16 Turbine Engine Inlet Flow Distortion Committee. A methodology for assessing inlet swirl distortion, b.
- [27] Bohn, D. and Simon, H. Mehrparametrische approximation der eichräume und eichflächen von unterschall-bzw. überschall-5-loch-sonden, *tm-Technisches Messen*, 1975, **4680**, (JG), pp 81–89.